The Astrophysical Journal Letters, 786:L16 (7pp), 2014 May 10 doi:10.1088/2041-8205/786/2/L16

NONLINEAR FORCE-FREE FIELD EXTRAPOLATION OF A CORONAL MAGNETIC FLUX ROPE SUPPORTING A LARGE-SCALE SOLAR FILAMENT FROM A PHOTOSPHERIC VECTOR MAGNETOGRAM

Chaowei Jiang[1,2], S. T. Wu[1], Xueshang Feng[2], and Qiang Hu[1]
[1] Center for Space Plasma and Aeronomic Research, The University of Alabama in Huntsville, Huntsville, AL 35899, USA; cwjiang@spaceweather.ac.cn, wus@uah.edu, qh0001@uah.edu
[2] SIGMA Weather Group, State Key Laboratory for Space Weather, Center for Space Science and Applied Research, Chinese Academy of Sciences, Beijing 100190, China; fengx@spaceweather.ac.cn
Received 2014 February 20; accepted 2014 April 3; published 2014 April 16

ABSTRACT

Solar filaments are commonly thought to be supported in magnetic dips, in particular, in those of magnetic flux ropes (FRs). In this Letter, based on the observed photospheric vector magnetogram, we implement a nonlinear force-free field (NLFFF) extrapolation of a coronal magnetic FR that supports a large-scale intermediate filament between an active region and a weak polarity region. This result is a first, in the sense that current NLFFF extrapolations including the presence of FRs are limited to relatively small-scale filaments that are close to sunspots and along main polarity inversion lines (PILs) with strong transverse field and magnetic shear, and the existence of an FR is usually predictable. In contrast, the present filament lies along the weak-field region (photospheric field strength $\lesssim$100 G), where the PIL is very fragmented due to small parasitic polarities on both sides of the PIL and the transverse field has a low signal-to-noise ratio. Thus, extrapolating a large-scale FR in such a case represents a far more difficult challenge. We demonstrate that our CESE–MHD–NLFFF code is sufficient for the challenge. The numerically reproduced magnetic dips of the extrapolated FR match observations of the filament and its barbs very well, which strongly supports the FR-dip model for filaments. The filament is stably sustained because the FR is weakly twisted and strongly confined by the overlying closed arcades.

Key words: magnetic fields – magnetohydrodynamics (MHD) – methods: numerical – Sun: corona – Sun: filaments, prominences

Online-only material: color figures

1. INTRODUCTION

Filaments are thin structures consisting of cool, dense plasma suspended in the tenuous hot corona. They lie above polarity inversion lines (PILs) on the photosphere and are formed in filament channels where the chromospheric fibrils are aligned with the PIL (Gaizauskas et al. 1997). Filaments can be found inside active regions (ARs; "AR filaments"), at the border of ARs ("intermediate filaments"), and on the quiet Sun ("quiescent filaments"). Most filaments eventually erupt and lead to coronal mass ejections, which are major drivers of space weather (Schmieder & Aulanier 2012).

The magnetic field plays a primary role in all coronal processes, including filament formation since the plasma β is low. It is now commonly accepted that filament plasma is supported in magnetic dips, in particular, within twisted flux ropes (FRs; e.g., Rust & Kumar 1994; Chae et al. 2001; van Ballegooijen 2004). Obtaining the three-dimensional (3D) magnetic field that supports filaments is key to understanding their structure, stability, and eruption. Unfortunately, the 3D coronal field is very difficult to measure directly. Thus people seek numerical models to construct the coronal field involved with filaments. The first numerical model was developed by Aulanier & Demoulin (1998) using linear force-free field extrapolation from a line-of-sight (LoS) magnetogram, which has proven to be a powerful tool to simulate filaments and related small structures like filament barbs (Aulanier & Demoulin 1998; Aulanier et al. 1998, 2000; Aulanier & Schmieder 2002; Dudik et al. 2008, 2012). Van Ballegooijen (2004) then developed a nonlinear force-free field (NLFFF) model, the FR insertion method, in which an FR with its axis following the targeted filament channel is first inserted into a potential field environment and the system is then relaxed to force-free equilibrium. The FR insertion method has been applied to modeling various filaments (e.g., van Ballegooijen 2004; Bobra et al. 2008; Su et al. 2011; Su & van Ballegooijen 2012; Savcheva et al. 2012).

NLFFF extrapolation from photospheric vector magnetograms (VMs) is a more general method used to reconstruct the coronal field (Sakurai 1981; Wu et al. 1990; Amari et al. 1997; Wiegelmann & Sakurai 2012), regardless of the presence of filaments. Unlike the FR insertion method, the NLFFF extrapolation can reconstruct an FR naturally and in a straightforward manner, if it exists. Recent studies have reported many examples with FRs extrapolated from different VMs using various NLFFF codes (e.g., Yan et al. 2001; Régnier & Amari 2004; Canou & Amari 2010; Cheng et al. 2010; Guo et al. 2010; Jing et al. 2010; Jiang & Feng 2013). Some studies also show that the extrapolated FR structure matches the related filament, e.g., good spatial correlation of the FR dips with the filament channels (Canou & Amari 2010; Guo et al. 2010). We note that all these works are limited to relatively small-scale filaments (lengths within tens of megameters) whose channels are close to sunspots and along the main PIL with strong transverse field and magnetic shear. In such cases, the existence of an FR is usually predictable by inspecting the VM. The sheared PIL, even with bald patches[3], usually indicates the presence of a coronal FR (Titov & Démoulin 1999; Aulanier et al. 2010). On the

[3] Places on the PIL where the transverse field is so strongly sheared that it points from the negative to the positive polarity, which is the opposite of a potential field case (Titov & Démoulin 1999).

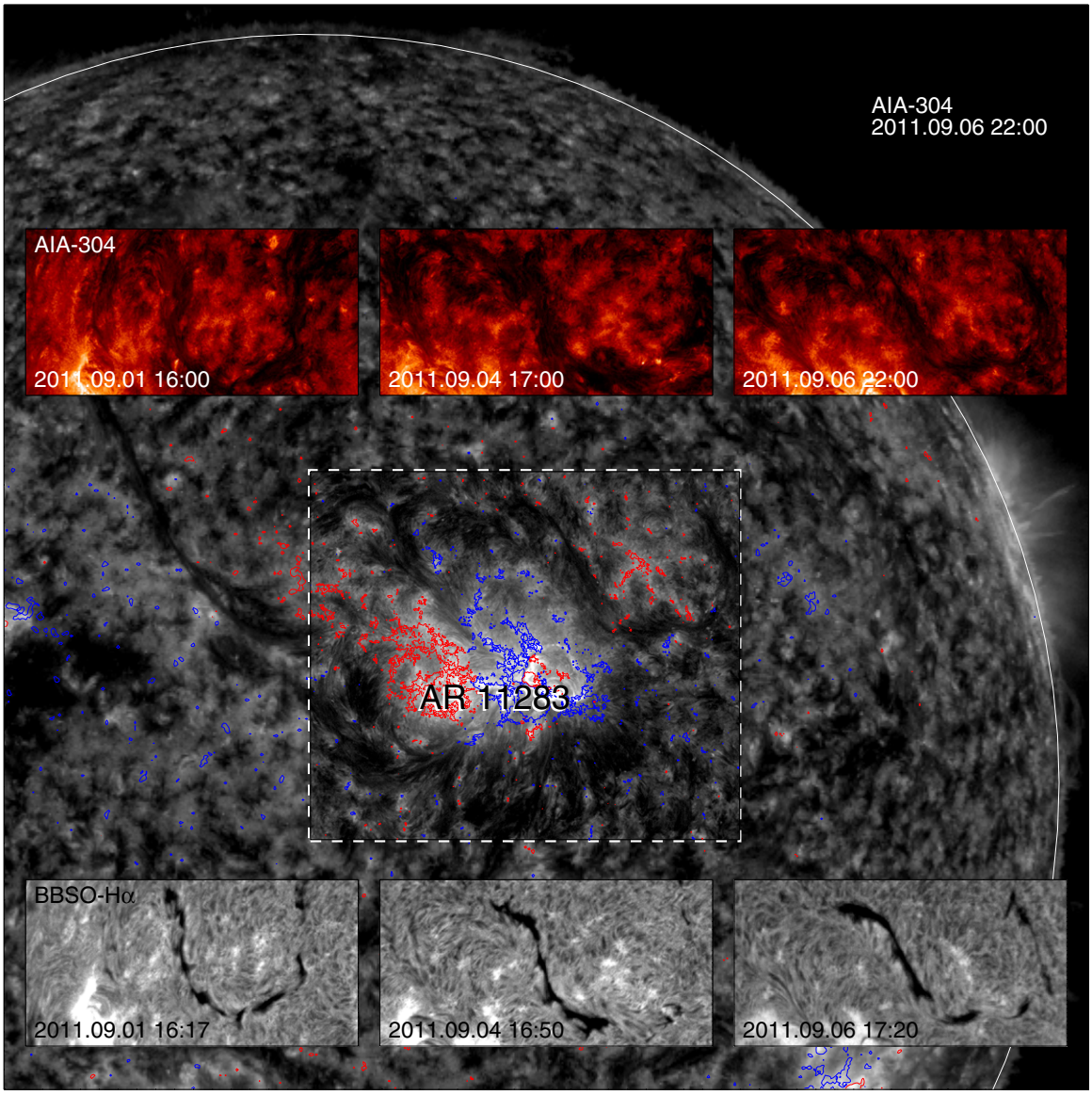

Figure 1. Background shows a large AIA-304 image at 22:00 UT on September 6, overlaid with contours of ±100 G (red/blue) for the LoS photospheric magnetic field. The white arc is the solar limb. The dashed box denotes the FoV of the VM used for extrapolation (see Figure 2). The inserted panels are observations of the filament channels in AIA-304 and the Hα filament at different times.

(A color version of this figure is available in the online journal.)

contrary, many large-scale filaments (lengths up to hundreds of megameters), like the intermediate and quiescent filaments, usually lie above the photospheric weak-field region (field strength $\lesssim$100 G), where the PIL is very fragmented due to small parasitic polarities on both sides and the transverse field is very noisy. As a result, the signature of an FR, e.g., unbroken PIL with strong magnetic shear, is difficult to observe directly from the magnetogram. Thus in such conditions, it is far more of a challenge to extrapolate a large-scale FR from the currently observed VM.

In this Letter, we report such a challenging NLFFF extrapolation that recovers a large-scale FR supporting an intermediate filament with a length up to 300 Mm. The extrapolation is based solely on the *SDO*/HMI VM without any other observation or artificial input. The extrapolation reproduces a coronal FR matching the filament recorded by the Atmospheric Imaging Assembly (AIA) and Hα strikingly well, which strongly supports the FR dip model for filaments. We further study why the FR can keep its stability during eruption.

2. OBSERVATIONS

A sigmoidal filament was observed to the northwest of AR 11283 during its passage through the solar disk. Figure 1 shows the observations in BBSO Hα and *SDO*/AIA-304. The filament first appeared at the east limb on 2011 August 30. It may have been formed before rotating into the visible disk. The main body of the filament seen in Hα shows a slightly inverse-S shape with a length of about 200 Mm. The filament channel is more extended, as observed by AIA, roughly forming a horizontally lying, fully inverse-S shape. The filament channel's west part is much more evident than the east part which appears rather fragmented. The filament was stable for days and partially erupted early on September 8 when approaching the west limb. Before its eruption, although the Hα filament evolved, the large-scale shape of the filament channel showed almost no clear change. This behavior suggests that the basic underlying magnetic structure is very stable.

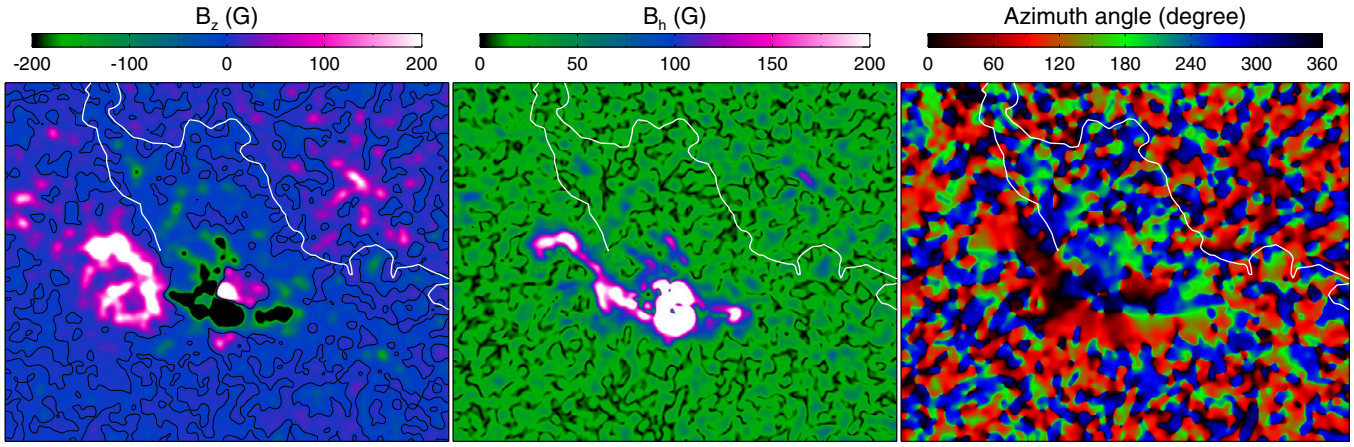

Figure 2. HMI VM at 22:00 UT on September 6. Its FoV is outlined by the dashed box in Figure 1. From left to right are the vertical field strength, horizontal field strength, and azimuthal angle, respectively. The map shown here is Gaussian-smoothed from the original data with an FWHM of 10 arcsec. The photospheric PILs are shown by the black contours in the left panel. The thick white lines overlaid on the maps are the PIL derived from the potential field extrapolated to a height of 10 arcsec, and only the part along the filament channel is shown.

(A color version of this figure is available in the online journal.)

The Hα observations show that there are barbs along the filament's main body, and most of them are right-bearing. This indicates the filament's chirality as dextral, meaning that the axial magnetic field in the filament points to the right when viewed from the side with positive polarity in the photosphere (Pevtsov et al. 2003). It can be seen from Figure 1 that the photospheric field in the southeast of the filament is predominantly negative and in the northwest predominantly positive. Hence according to the chirality, the axial field in the filament's main body would point to the northeast. We will discuss more details of the filament structure with the help of the extrapolated coronal field.

3. RESULTS

Here we only show the NLFFF extrapolation at 22:00 UT on September 6. This moment interests us because there is a sigmoid eruption from AR 11283, which was previously studied in Jiang et al. (2013, 2014), and obtaining the large-scale coronal field around this moment will improve our understanding of the sigmoid eruption. Figure 2 shows the VM. It has a field of view (FoV) of 600 $\times$ 480 arcsec^2, which is large enough to include almost the whole filament channel (except that the west end of the channel is outside of the FoV). The magnetogram as shown has been Gaussian-smoothed with an FWHM of 10 arcsec since the original data is much noisier. However, we find that the photospheric PILs are still too fragmented to identify where the filament is located above. To establish a reasonable PIL that follows the filament channel, we overlay on the maps the potential-field PIL computed at a small height (10 arcsec) above the photosphere, which is much more extended than the photospheric PIL because the small polarities decay fast with height. As can be seen along this PIL that represents the path of the EUV filament channel, the transverse field is rather weak ($\leqslant$100 G), and its directions show a rather random pattern without systematic magnetic shear regarding the length scale of the filament.

The extrapolation is carried out using our CESE–MHD–NLFFF code in exactly the same way as Jiang & Feng (2013), without any parameter optimized for the present modeling. The code is based on the MHD relaxation method and implemented by an advanced conservation-element/solution-element (CESE) spacetime scheme on an adaptive grid with parallel computation (Jiang et al. 2010). Before inputting to the extrapolation code, the original VM is preprocessed to remove the photospheric Lorentz force using a new preprocessing method (Jiang & Feng 2014). We compute the field in a Cartesian box of 768 $\times$ 640 $\times$ 384 arcsec^3 (with a resolution of 1 arcsec), which includes a peripheral region around the VM.[4]

3.1. Extrapolation Result and Comparison with Observations

Figure 3 compares the extrapolation result with AIA and Hα observations. The top-right panel shows the magnetic field lines. The angle of view is co-aligned approximately with the *Solar Dynamics Observatory* (*SDO*). The black field lines are plotted to represent the coronal loops observed in AIA-171. Along the filament channel, there is indeed an FR, which is shown by the colored rod-like lines, with the color denoting the height from the photosphere as indicated by the color bar. As can be seen, the middle of the FR is low-lying at about 20–40 Mm, while its two ends are high reaching and close to arcades. There is some flux of the rope passing through the west boundary, possibly because the FoV of the magnetogram does not fully include the entire FR system. Overall, the rope presents an inverse-S shape roughly matching the filament channel, and its chirality is correctly reproduced. It is interesting to find that some field lines from the AR's sunspot turn into the FR. Overlying the FR is a group of potential-like field lines, and only the two ends of these field lines are visible as bright rays in the AIA-171 image, because the emission drops off rapidly with height. This overlying closed arcade is expected to play a key role in stabilizing the FR.

The middle-right panel of Figure 3 shows the magnetic dips, i.e., the locations where the field lines are locally horizontal ($B_z = 0$) and curved upward ($\boldsymbol{B} \cdot \nabla B_z \geqslant 0$). The dips are also pseudo-colored by the height. In the last two right panels of Figure 3, we plot the horizontal field vectors (using a uniform length of 1 Mm) at all of the dips to simulate the observed filament channel (van Ballegooijen 2004). Evidently, there is a long extended dip reaching above 30 Mm, reproducing very

[4] In principle, it would be better to compute the field in the spherical geometry for such a large FoV (Jiang et al. 2012), so the extrapolated field can be accurately co-aligned with observations.

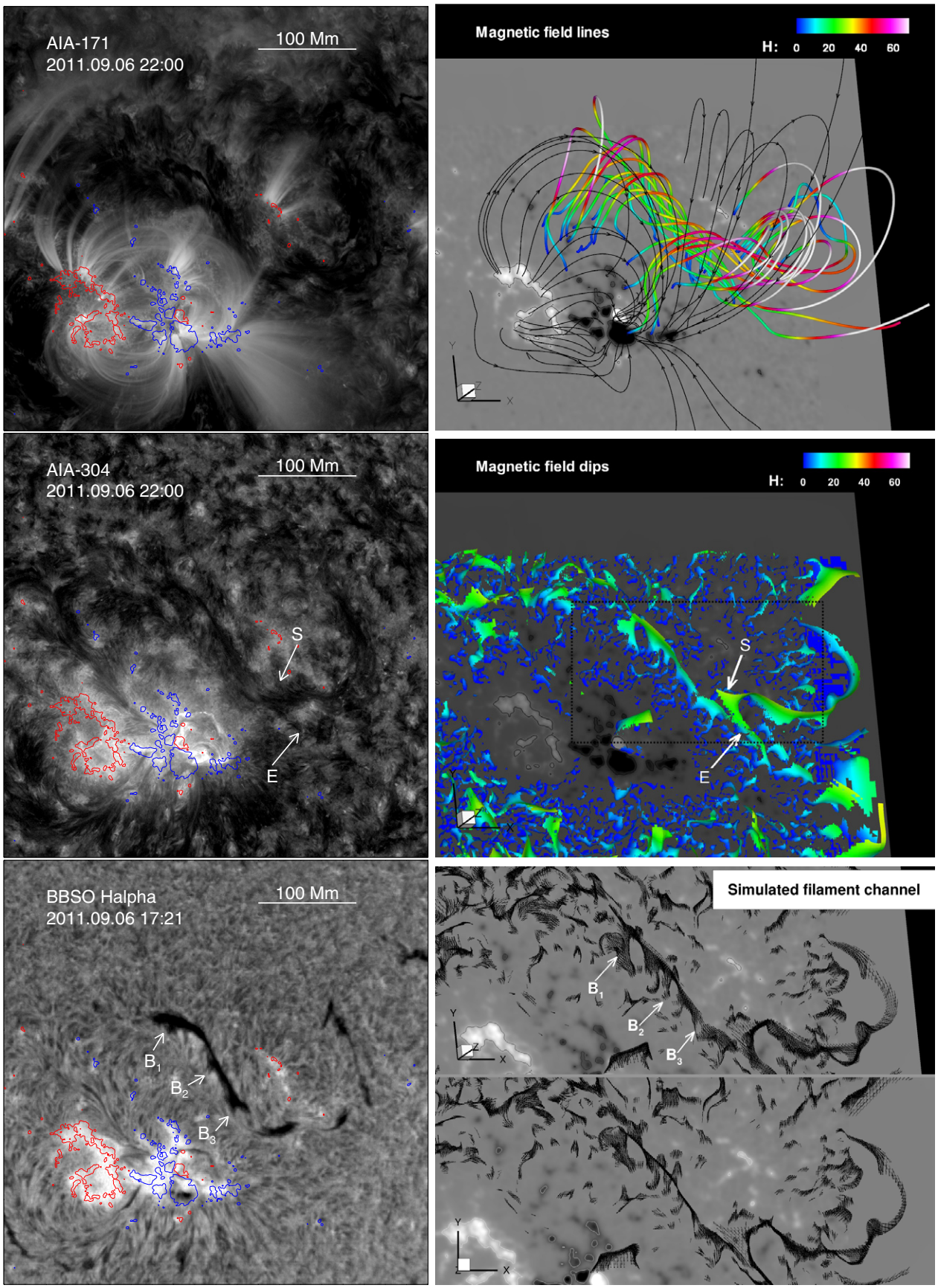

Figure 3. Left: observations of the filament channel by *SDO*/AIA and BBSO Hα. The overlaid contours are the LoS photospheric magnetic field (red for 200 G and blue for −200 G). Right: model results of the coronal field. The magnetogram of B_z is shown as the gray background. In the right panels on top and in the middle, the color represents the height from the bottom (in units of Mm). See the text for details.

(A color version of this figure is available in the online journal.)

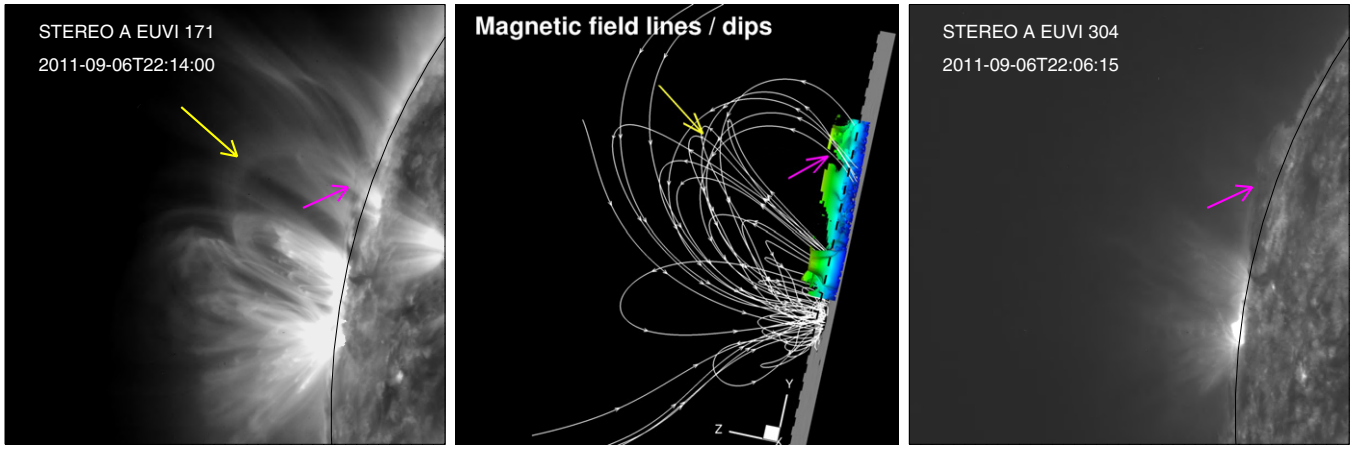

Figure 4. Left and right: *STEREO-A* observations of the prominence in EUVI-171 and EUVI-304, respectively. The black arcs are the solar limb. The pink arrow marks the prominence and the yellow arrow marks the overlying arcades. Middle: the coronal field lines model the EUVI-171 loops and magnetic field dips model the prominence, with the solar limb denoted by the dashed black line. Note that only the dips of the FR main body, i.e., those within the dashed box in middle right panel of Figure 3, are shown here.

(A color version of this figure is available in the online journal.)

well the main body of the filament (i.e., the middle section of the filament channel). Moreover, a sigmoidal channel, following the observed inverse S-shaped filament channel, can be seen from the dips, although the east end is very fragmented as in the case of the observation. The model does not reproduce well the west end of the filament channel because it is near the boundary of the magnetogram.

In the middle panels, as marked by the arrow *S*, it appears that the filament spine is interrupted by a north deviation of its west part from the main body, resulting in an elongated barb in the south side (marked by the arrow *E*). Our model recovers this offset and the elongated barb, which are caused by a local intrusion in the PIL by a group of strong positive polarities (>100 G, just at the site of the interruption; see Figure 1), locally altering the path of the FR. In addition, the right-bearing barbs along the filament's main body, as marked by the arrows B_1, B_2, and B_3, are reproduced by the model. As shown by the model result viewed from above (Figure 3, bottom right panel), there are also several "barbs" at the north side which are not seen in the observation because they were hidden behind the filament spine.

By inspecting the dips shown in the middle-right panel, we find that there is a large amount of localized fragmentation of dips (shown in deep blue) that is very close to and on the photosphere (i.e., bald patches). These dips result from the highly intermittent distribution of the photospheric field (Aulanier & Schmieder 2002; Dudik et al. 2008). The number of localized dips decreases very fast with height since the related small-scale fields decay fast with height. Around the AR, the model produces many dips of rather short extensions, and these dips may support the small-scale filaments as observed around the AR both in AIA and Hα. We note that high dips near the side boundaries should not be taken seriously because the magnetic field on those boundaries are fixed, and during NLFFF computing the field lines near the boundaries are squeezed to produce these artificial dips.

The filament was also observed by *STEREO-A* at the limb as a low-lying prominence. Figure 4 compares the *STEREO* observations with the model result, also shown in a limb view. The field lines compare the EUV bright loops and the dips represent the prominence. As viewed by *STEREO-A*, a closed arcade (marked by a yellow arrow) overlying the prominence is clearly observed in the EUVI-171. This arcade corresponds to the potential-like field lines, two ends of which are visible in AIA-171. The prominence reaches its highest point (about 30 Mm) in the north, then smoothly descends along its path to the south, and its spine turns into the solar disk. The modeled magnetic dips correctly reproduce the height profile of the observed prominence, except that near the south end the simulated prominence appears much higher than the observed one. We attribute such disagreement to several reasons: first, the model does not construct properly the west end of the filament channel because it is beyond the FoV of the magnetogram; second, the model is constructed in a Cartesian box, and as a result the curvature of the long filament channel is not well characterized; last, the magnetic dips do not necessarily represent the prominence if they are not filled with the cold prominence plasma.

3.2. Stability of the FR

It is known that a coronal FR confined by an overlying potential arcade is subject to two kinds of instabilities, i.e., kink instability (KI) and torus instability (TI). KI states that an FR will deform helically if the twist degree, which is measured by the number of windings of the field lines around the rope axis, exceeds a critical value (about 1.5–2, Török & Kliem 2005). TI occurs when the outward expansion of an FR can no longer be confined by the overlying field if it decays faster than an unstable threshold, which is characterized by a decay index of the external field with an unstable threshold of ~1.5 (Kliem & Török 2006).

In Figure 5(a), we show several field lines around the FR's axis with different colors. These field lines pass through the central cross section of the FR, as shown in Figure 5(b), and the rope axis is located at the center of the helical shapes formed by the poloidal flux of the rope. Note that in Figure 5(b), the background shows the magnetic field strength. It can clearly be seen that the field strength is enhanced in the rope region because of the strong axial flux of the rope. The cross section of the field dips (the thick blue curved line) starts from the FR axis and reaches down to the photosphere. The FR is tilted to the right due to the non-symmetry of the flux distribution.

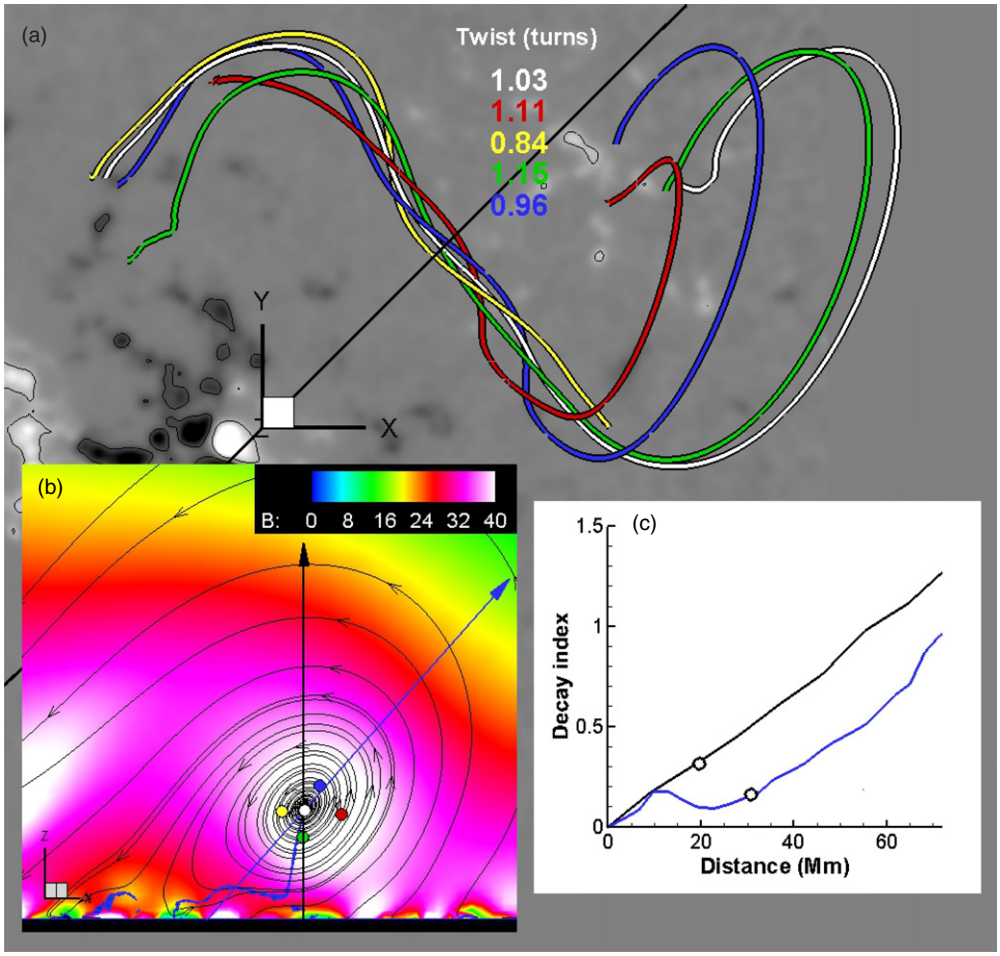

Figure 5. (a) Four sampled field lines (blue, red, green, and yellow, respectively) around the FR axis (white). The colored numbers denote the twist degrees of these field lines. (b) Central cross section of the FR, which is vertically sliced along the black line shown in panel (a). The streamlines show the 2D field-line tracing on the slice, which forms helical lines centered at the axis of the FR. The background shows the magnetic field strength (in units of G). The small colored circles denote the locations of the field lines shown in panel (a). Note that the blue, thick curved lines consist of the magnetic dips. The two lines directed through the helix center (i.e., the FR axis) represent the paths along which we calculate the decay index. Distributions of the decay index along these two paths (starting from the bottom) are displayed in panel (c), and the locations of the rope axis are marked by the circles on the lines of the decay index.

(A color version of this figure is available in the online journal.)

Consequently, the field dips are not aligned vertically, but with a small deviation of $\sim 10^{\circ}$ from the vertical. Due to a localized parasitic polarity intrusion at the photosphere PIL, the dips reaching the bottom are strongly deflected almost in a horizontal way, naturally producing a lateral foot, i.e., a barb of the filament (Aulanier & Demoulin 1998).

The twist degree of the FR is computed according to (Inoue et al. 2011), $T_n = \int \alpha dl/(4\pi)$, where T_n corresponds to the number of turns of the magnetic field line, α is the force-free parameter, and the integral $\int dl$ is taken along the magnetic field line. The result shows that the field lines make about one turn (see Figure 5(a)), which is clearly less than the threshold for KI. To test if TI can occur, we compute the decay index of the potential field in the central cross section. The decay index is calculated along two different lines through the rope axis, a vertical line and an inclined line that is approximately along the inclination of the overlying arcade. Note that only the component of the potential field perpendicular to the directions is used (Jiang et al. 2014). Figure 5(c) shows the result, and the location of the rope axis is marked by circles on the profile lines of the decay index. Clearly, the FR is far below the height with a TI threshold, i.e., 1.5. So the FR is very strongly confined by its overlying flux, and a slow evolution of the photospheric field is not likely to trigger the filament eruption on September 8. We suggest that it is instructive to study the eruption in the context of the interaction between the AR eruption and the filament.

4. CONCLUSIONS

This Letter reports an NLFFF extrapolation of the solar coronal field that holds a large-scale filament from photospheric VM, which provides concrete evidence for filaments being supported by magnetic FR. Although the presence of a large-scale FR can hardly be predicted from the noisy VM, our CESE–MHD–NLFFF extrapolation code is able to overcome this difficulty to extract the key information of the coronal field from the magnetogram. We have also examined the robustness of the extrapolation by using VMs at two other times nearby (not shown here), which also reproduce a similar FR structure. A detailed comparison with multiple observations, including those of stereoscopic viewpoints, demonstrates that the filament structure is well reproduced by the extrapolation. The FR that supports the filament is very stable because it is weakly twisted and strongly confined by the overlying closed arcades. Its eruption is likely triggered by a nearby AR eruption, which requires further investigation.

This work is supported by NSF-AGS1153323 and AGS1062050. In addition, C.W.J. and X.S.F. are also supported by the 973 program under grant 2012CB825601, the Chinese Academy of Sciences (KZZD-EW-01-4), the National Natural Science Foundation of China (41204126, 41231068, 41274192, 41031066, and 41374176), and the Specialized Research Fund for State Key Laboratories. Data from observations are courtesy of NASA *SDO*/AIA and the HMI science teams.

REFERENCES

Amari, T., Aly, J. J., Luciani, J. F., Boulmezaoud, T. Z., & Mikic, Z. 1997, SoPh, 174, 129
Aulanier, G., & Demoulin, P. 1998, A&A, 329, 1125
Aulanier, G., Demoulin, P., van Driel-Gesztelyi, L., Mein, P., & DeForest, C. 1998, A&A, 335, 309
Aulanier, G., & Schmieder, B. 2002, A&A, 386, 1106
Aulanier, G., Srivastava, N., & Martin, S. F. 2000, ApJ, 543, 447
Aulanier, G., Török, T., Démoulin, P., & DeLuca, E. E. 2010, ApJ, 708, 314
Bobra, M. G., van Ballegooijen, A. A., & DeLuca, E. E. 2008, ApJ, 672, 1209
Canou, A., & Amari, T. 2010, ApJ, 715, 1566
Chae, J., Wang, H., Qiu, J., et al. 2001, ApJ, 560, 476
Cheng, X., Ding, M. D., Guo, Y., et al. 2010, ApJL, 716, L68
Dudik, J., Aulanier, G., Schmieder, B., Bommier, V., & Roudier, T. 2008, SoPh, 248, 29
Dudik, J., Aulanier, G., Schmieder, Zapior, M., & Heinzel, P. 2012, ApJ, 761, 9
Gaizauskas, V., Zirker, J. B., Sweetland, C., & Kovacs, A. 1997, ApJ, 479, 448
Guo, Y., Schmieder, B., Démoulin, P., et al. 2010, ApJ, 714, 343
Inoue, S., Kusano, K., Magara, T., Shiota, D., & Yamamoto, T. T. 2011, ApJ, 738, 161
Jiang, C., & Feng, X. 2013, ApJ, 769, 144
Jiang, C., & Feng, X. 2014, SoPh, 289, 63
Jiang, C., Feng, X., & Xiang, C. 2012, ApJ, 755, 62
Jiang, C., Feng, X., Zhang, J., & Zhong, D. 2010, SoPh, 267, 463
Jiang, C. W., Feng, X. S., Wu, S. T., & Hu, Q. 2013, ApJL, 771, L30
Jiang, C. W., Wu, S. T., Feng, X. S., & Hu, Q. 2014, ApJ, 780, 55
Jing, J., Yuan, Y., Wiegelmann, T., et al. 2010, ApJL, 719, L56
Kliem, B., & Török, T. 2006, PhRvL, 96, 255002
Pevtsov, A. A., Balasubramaniam, K. S., & Rogers, J. W. 2003, ApJ, 595, 500
Régnier, S., & Amari, T. 2004, A&A, 425, 345
Rust, D. M., & Kumar, A. 1994, SoPh, 155, 69
Sakurai, T. 1981, SoPh, 69, 343
Savcheva, A., Pariat, E., van Ballegooijen, A., Aulanier, G., & DeLuca, E. 2012, ApJ, 750, 15
Schmieder, B., & Aulanier, G. 2012, AdSpR, 49, 1598
Su, Y., Surges, V., van Ballegooijen, A., DeLuca, E., & Golub, L. 2011, ApJ, 734, 53
Su, Y., & van Ballegooijen, A. 2012, ApJ, 757, 168
Titov, V. S., & Démoulin, P. 1999, A&A, 351, 707
Török, T., & Kliem, B. 2005, ApJL, 630, L97
van Ballegooijen, A. A. 2004, ApJ, 612, 519
Wiegelmann, T., & Sakurai, T. 2012, LRSP, 9, 5
Wu, S. T., Sun, M. T., Chang, H. M., Hagyard, M. J., & Gary, G. A. 1990, ApJ, 362, 698
Yan, Y., Deng, Y., Karlický, M., et al. 2001, ApJL, 551, L115